PAPER

Check for updates

Role of processing parameters in CVD grown crystalline monolayer MoSe$_2$†

Girija Shankar Papanai,[ab] Krishna Rani Sahoo,[c] Betsy Reshma G,[bd] Sarika Gupta[e] and Bipin Kumar Gupta [ID] *[ab]

The quality of as-synthesized monolayers plays a significant role in atomically thin semiconducting transition metal dichalcogenides (TMDCs) to determine the electronic and optical properties. For designing optoelectronic devices, exploring the effect of processing parameters on optical properties is a prerequisite. In this view, we present the influence of processing parameters on the lattice and quasiparticle dynamics of monolayer MoSe$_2$. The lab-built chemical vapour deposition (CVD) setup is used to synthesize monolayer MoSe$_2$ flakes with varying shapes, including sharp triangle (ST), truncated triangle (TT), hexagon, and rough edge circle (REC). In particular, the features of as-synthesized monolayer MoSe$_2$ flakes are examined using Raman and photoluminescence (PL) spectroscopy. Raman spectra reveal that the frequency difference between the A$_{1g}$ and E$_{2g}^1$ peaks is >45 cm^{-1} in all the monolayer samples. PL spectroscopy also shows that the synthesized MoSe$_2$ flakes are monolayer in nature with a direct band gap in the range of 1.50–1.58 eV. Furthermore, the variation in the direct band gap is analyzed using the spectral weight of quasiparticles in PL emission, where the intensity ratio $\{I(A^0)/I(A^-)\}$ and trion binding energy are found to be ~1.1–5.0 and ~23.1–47.5 meV in different monolayer MoSe$_2$ samples. Hence, these observations manifest that the processing parameters make a substantial contribution in tuning the vibrational and excitonic properties.

Introduction

Ultrathin two-dimensional transition metal dichalcogenides (2D-TMDCs) have attracted considerable attention over the past few years owing to their fascinating physical and chemical properties.[1] The broader electron orbitals of selenide (Se^{2-}) in comparison to sulfide (S^{2-}) open up new avenues for numerous applications in the field of optoelectronics,[2,3] logic circuits,[4] and tunnel FET technology.[5] Bulk MoSe$_2$ has an indirect band gap of ~1.1 eV and crossovers into a direct band gap of ~1.55 eV in its monolayer form.[6]

There are various methods to synthesize monolayer and few-layer MoSe$_2$, including mechanical exfoliation, liquid-phase exfoliation, ion insertion, molecular beam epitaxy,

hydrothermal methods, and chemical vapor deposition.[7,8] Among these, chemical vapor deposition is one of the preferred methods which provides high quality, large area, uniform thickness, and desired morphology of MoSe$_2$ flakes.[9–11] However the optimization of monolayer MoSe$_2$ becomes challenging due to poor chemical reactivity of selenium (Se) in comparison to sulfur (S). Generally, solid precursors are converted into the vapor phase during CVD growth of 2D-TMDCs, and deposited over the substrate in the solid form *via* molecular transport and surface diffusion processes. Recently, Kim *et al.* synthesized monolayer MoSe$_2$ using a promoter assisted liquid phase CVD process in which ammonium orthomolybdate [(NH$_4$)$_2$MoO$_4$] was used as a transition metal-containing precursor and potassium iodide (KI) as a promoter.[12] In another study, metal chlorides, *i.e.*, CaCl$_2$ and SrCl$_2$, were used as promoters to grow monolayer MoSe$_2$.[13] In addition to this, mm-size monolayer MoSe$_2$ has been synthesized on a soda-lime glass substrate using a beam bridge transition metal precursor supply by another research group.[14] Nevertheless, there are some drawbacks to using promoters for large-area synthesis, which include doping, and the formation of a metal oxide layer underneath the monolayer TMDCs.[15,16]

To resolve such complications, promoter-free growth has been taken into consideration in the present work. Next, in photoluminescence study of CVD-grown monolayer MoSe$_2$, the peak position of A exciton varies from ~1.48–1.57 eV in earlier

*a*Photonic Materials Metrology Sub Division, Advanced Materials and Device Metrology Division, CSIR-National Physical Laboratory, Dr K. S. Krishnan Marg, New Delhi 110012, India. E-mail: bipinbhu@yahoo.com

*b*Academy of Scientific and Innovative Research (AcSIR), Ghaziabad 201002, India

*c*Tata Institute of Fundamental Research – Hyderabad, Sy. No. 36/P Serilingampally, Mandal, Gopanpally Village, Hyderabad 500046, India

*d*CSIR-Institute of Genomics and Integrative Biology, Mathura Road, New Delhi 110025, India

*e*Molecular Sciences Lab, National Institute of Immunology, Aruna Asaf Ali Marg, New Delhi 110067, India

† Electronic supplementary information (ESI) available. See https://doi.org/10.1039/d2ra00387b

reports.[9,10,17,18] The variation in PL peak position directly affects nature of quasiparticles. In monolayer TMDCs, the quasiparticle dynamics play a significant role due to reduced dielectric screening, strong quantum confinement, and the larger effective masses of charge carriers. In a semiconductor, the fundamental optical excitation is electron–hole (e–h) pair which is bounded *via* Coulomb attraction called an exciton. The binding energy of exciton and trion is larger in monolayer TMDCs as compared to quasi 2D semiconductors, namely GaAs quantum well, which makes these carriers stable at ambient temperature. There are several reports on the quasiparticles dynamics and exciton–trion interaction in monolayer $MoSe_2$.[19–22] But influence of experimental parameters on the behavior of quasiparticles is still missing. To explain this, quasiparticles behavior has been examined at different growth conditions using PL emission spectroscopy.

In this work, we report the synthesis of high-quality monolayer $MoSe_2$ flakes using a lab-built CVD setup at atmospheric pressure. The lattice dynamics and charge carrier features have been studied in detail under the influence of processing parameters in as-synthesized samples and as-obtained shapes. To the best of our knowledge, influence of experimental parameters on Raman scattering and PL in CVD-grown monolayer $MoSe_2$ flakes is not reported yet.

Experimental section

Synthesis of $MoSe_2$ flakes

The monolayer $MoSe_2$ flakes have been synthesized using lab-built CVD setup in a single zone furnace. This lab-built CVD setup has also been used to synthesize the monolayer MoS_2 flakes in our previous work.[23] Prior to synthesis, SiO_2/Si (300 nm) substrates are sonicated in acetone and isopropyl alcohol (IPA) for 10 min each to remove the surface adsorbates. Further, the substrates have been rinsed with deionized water followed by HF dip (2%) and blow-dried using N_2 gas. For the reaction, solid precursors molybdenum(VI) oxide (MoO_3) powder (>99%, Fisher Scientific) and selenium (Se) pellets (99.999%, CERAC) have been loaded along with SiO_2/Si substrate inside the quartz tube (ID 60 mm × OD 65 mm × *L* 1200 mm). The MoO_3 powder (15–30 mg) has been placed in alumina boat (length ∼ 9 cm) at the center of split tube furnace. Se pellets (153–305 mg) have been kept in second alumina boat at a separation of ∼20 cm from MoO_3 powder on upstream side of furnace. The Si/SiO_2 substrates have been kept upside down above MoO_3 powder's loaded alumina boat towards the downstream side. The reaction chamber has been pumped down up to a base pressure of ∼2.8 × 10^{-2} mbar and purged with high purity Ar gas for half an hour. After purging, H_2 (10–25 sccm) and Ar (60–200 sccm) gases have been introduced in the reaction chamber at atmospheric pressure and constantly maintained till the cooling process. The temperature of furnace has been heated gradually up to 770–810 °C within 70 min and hold for 15–32 min. After the growth, furnace has been opened at 600 °C and allowed to cool naturally in the presence of Ar and H_2 gas up to 100 °C. After cooling, samples have been taken out and used for further characterizations.

Transfer of $MoSe_2$ flakes on TEM grid

The $MoSe_2$ flakes are transferred on holey carbon Cu TEM grid using HF. The shiny/dark side of TEM grid is put over Si/SiO_2 substrate in the region where flakes need to be transferred. The 5% HF solution is drop casted on the region of TEM grid using a micropipette and wait for 30 s. After this step, the TEM grid with $MoSe_2$ flakes has soaked in DI water for several times and dried at ambient condition.

Characterization

The XRD system Rigaku (MiniFlex II) is used to record the diffraction pattern of MoO_3 and Se precursors with Cu $K\alpha_1$ (λ = 1.5418 Å) as a radiation source. Optical microscopy has been used to visualize the synthesized $MoSe_2$ monolayer over Si substrate having a SiO_2 thickness of 300 nm (GMS-India). The LEXT 3D measuring laser microscope OLS5100 has been used in the bright field mode with objective lenses MPLAPON50XLEXT, MPLAPON100XLEXT having NA, and the working distance of 0.95 and 0.35 mm, respectively. Additionally, Leica DM 2700M equipped with Raman microscope has also been used to capture optical images in bright field mode with 50× and 100× magnification. Further, the surface morphologies of synthesized $MoSe_2$ flakes have been probed using scanning electron microscopy (FESEM Model: JEOL, JSM-7200F) under an acceleration voltage of 5–25 kV. For measuring the thickness of $MoSe_2$ flakes, atomic force microscope (AFM Model: Keysight 5500) has been used in contact mode. The TEM images and diffraction patterns have been captured with FEI Tecnai TF20 (accelerating voltage: 200 kV) equipped with a field-emission gun (FEG) source and a 4k × 4k Eagle CCD Camera. The chemical states are examined at room temperature using ESCA+ (Omicron Nanotechnology, Oxford Instrument Germany) equipped with monochromatic Al $K\alpha$ source ($h\nu$ = 1486.7 eV). The binding energy of C 1s core (284.6 eV) is taken as a reference, and a charge neutralizer of 2 keV is applied to overcome the charging problem. UV-visible absorption spectrum of the $MoSe_2$ flakes has been recorded using a UV-vis spectrometer (AvaLight-DH-S-BAL) to study the optical transitions. Raman and PL measurements have been employed using the Renishaw inVia™ confocal Raman microscope with 50× magnification at ambient condition. The Raman spectra have been recorded using an excitation laser wavelength of 532 nm, having the power of 2.5 mW under exposure time of 10 s with 2400 l mm^{-1} grating, respectively. The PL spectra have been captured using an excitation wavelength of 633 nm having laser power of 5 mW under exposure time of 10 s with 1800 l mm^{-1} grating, respectively.
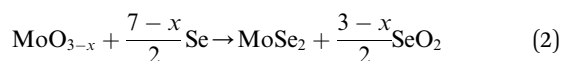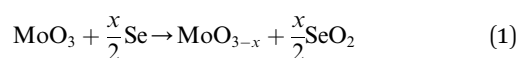
Results and discussion

The monolayer $MoSe_2$ flakes have been synthesized using the lab-built CVD setup in a single zone furnace. The schematic diagram of synthesis of $MoSe_2$ flakes using solid MoO_3 and Se precursors by the CVD method has been shown in Fig. S1 in the ESI,† where the notations are in their usual meaning. Prior to synthesis, MoO_3 and Se precursors are also examined using

Table 1 The different samples of monolayer MoSe$_2$ flakes have been synthesized over Si/SiO$_2$ substrate at different optimized processing parameters

Sample name	Growth temperature (°C)	MoO$_3$ powder (mg)	Se pellets (mg)	H$_2$ flow (sccm)	Ar flow (sccm)	Deposition time (min)
MS-1	770	30	305	20	60	30
MS-2	770	20	252	15	60	20
MS-3	780	20	185	20	200	32
MS-4	780	15	155	20	60	20
MS-5	780	15	172	20	60	20
MS-6	790	15	153	15	60	20
MS-7	800	25	248	25	100	30
MS-8	810	30	302	10	60	15

XRD, as displayed in Fig. S2 (in the ESI).† Past study interpreted that the synthesis of monolayer MoSe$_2$ takes place only when H$_2$ gas is introduced in the reaction chamber.[24] Here, H$_2$ gas plays a key role in creating a reducing environment for MoO$_3$ in addition to Se and facilitates the growth of MoSe$_2$ monolayer. The formation of monolayer MoSe$_2$ occurs on the substrate *via* reaction of MoO$_3$ and Se in the presence of Ar and H$_2$ gas. With a similar analogy of MoS$_2$ formation, the plausible stepwise reaction can be expressed by the following equations:[25]

$$MoO_3 + \frac{x}{2}Se \rightarrow MoO_{3-x} + \frac{x}{2}SeO_2 \tag{1}$$

$$MoO_{3-x} + \frac{7-x}{2}Se \rightarrow MoSe_2 + \frac{3-x}{2}SeO_2 \tag{2}$$

Here, eqn (1) shows the reaction during the period of the heating ramp, and eqn (2) describes the reaction in the period of holding time of temperature during growth. To obtain high quality MoSe$_2$ monolayer, the number of processing parameters, namely gas flow rate, location of substrate, growth temperature, and growth time, need to be optimized. The best samples of as-synthesized monolayer MoSe$_2$ flakes on Si/SiO$_2$ substrate (MS-1 to MS-8) at different optimized conditions have been tabulated in Table 1. The optical images of different samples of monolayer MoSe$_2$ flakes over Si substrate having SiO$_2$ thickness of 300 nm have been illustrated in Fig. 1. The contrast variation in optical images appears due to the different optical settings of used microscopes. One can see the different
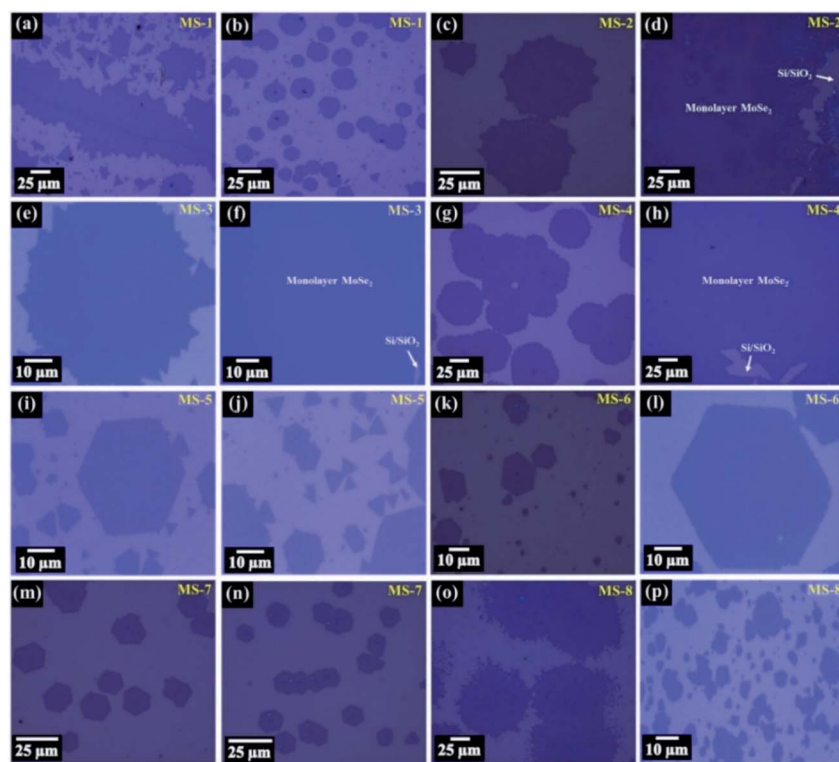

Fig. 1 The optical images of eight different CVD-grown monolayer MoSe$_2$ samples are named MS-1 to MS-8, deposited on Si substrate having SiO$_2$ thickness of 300 nm. (a and b) Sample MS-1. (c and d) Sample MS-2. (e and f) Sample MS-3. (g and h) Sample MS-4. (i and j) Sample MS-5. (k and l) Sample MS-6. (m and n) Sample MS-7. (o and p) Sample MS-8.
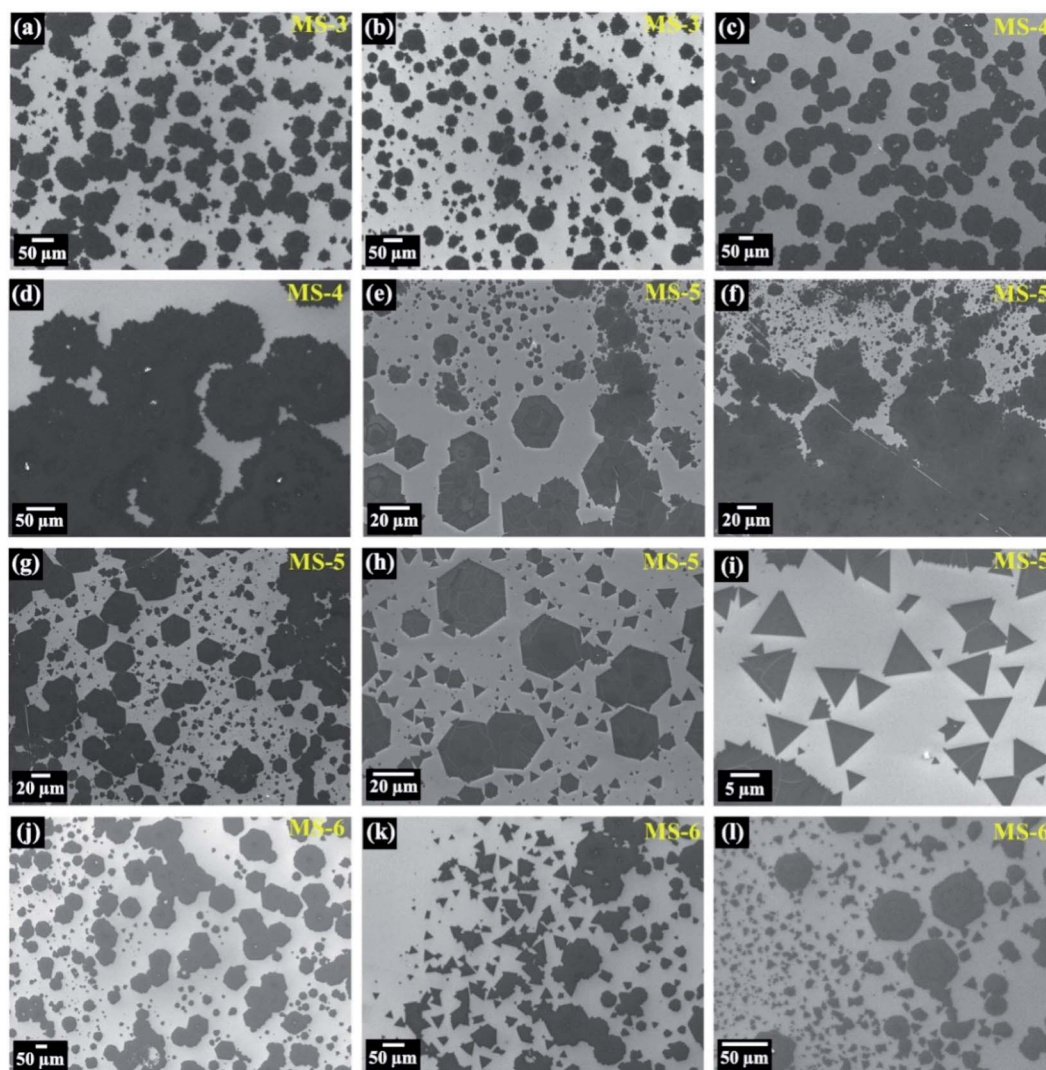
Fig. 2 SEM images of CVD grown monolayer $MoSe_2$ samples over Si/SiO_2 substrate: (a and b) sample MS-3. (c and d) Sample MS-4. (e–i) Sample MS-5. (j–l) Sample MS-6.

shapes of $MoSe_2$ flakes, namely sharp triangle (ST), truncated triangle (TT), hexagon, rough edge circle (REC), at varying experimental conditions. The large area deposition of $MoSe_2$ monolayer can be observed as well from Fig. 1d, f and h. Further, the morphological evolution of monolayer $MoSe_2$ flakes has also been explored using scanning electron microscopy (SEM). Fig. 2 displays the SEM images of four samples, *i.e.*, MS-3, MS-4, MS-5, and MS-6. These four samples are chosen for SEM measurements due to more coverage of individual shapes at one location over the Si/SiO_2 substrate. The SEM images of as-synthesized REC $MoSe_2$ flakes having non-uniform zig-zag (zz) edges are shown in Fig. 2a–d. Fig. 2e–i exhibits the SEM images of different shapes such as ST, TT, and hexagon, respectively. The as-synthesized different shapes in MS-5 are obtained at different locations on same substrate due to gradient in the evaporation rate of Mo and Se. Fig. 2j–l presents the SEM images of REC, ST, and hexagon shapes of monolayer $MoSe_2$. The precursor dynamics, which include evaporation, transport, and chemical reaction, determine the different shapes of $MoSe_2$

flakes. The different experimental conditions affect the process of edge diffusion and attachment of atoms. Therefore, shape of flakes is transformed into another shape according to their thermodynamic stability. As shown in Fig. 2, the sample MS-5 covers most of the region by high-quality single-crystal ST and hexagon flakes.

Next, the surface morphology of sample MS-4 shows identical REC shapes with high uniformity. It is generally known, the compactness of any shape is defined by the area to perimeter ratio, and the REC has the large compactness.

The formation of REC shape resulted from the high growth rate of both Mo and Se edges, suggesting that both edges have insufficient time to diffuse on the preferable location of the lattice. Under the Se rich atmosphere, Mo atoms have more probability of attaching with Se atom instead of another incoming Mo atom at the flake edge; enhance the lateral growth. One can notice from the surface morphologies that the nucleation takes place on substrate in a random manner. However, color contrast in each sample indicates that the

monolayer flakes are formed with high uniformity (see Fig. 1). After the nucleation process, monolayer growth takes place *via* attachment and diffusion of adsorbed atoms on substrate. Quantitatively, distribution of adsorbed atoms and the growth rate can be represented by the following diffusion equation:[26]

$$\frac{\partial c_n}{\partial t} = D_n \nabla^2 c_n + F_n - \frac{c_n}{\tau_{d,n}} \quad (3)$$

where c_n, D_n, F_n, and τ_d denote the number of adsorbed atoms, diffusion coefficient, adsorbed atoms supply rate, and effective lifetime of adsorbed atoms before desorption. By tuning the diffusion length $\lambda = \sqrt{D\tau_d}$ and adsorbed atom supply rate (F), the growth in lateral direction can be controlled. As the flow rate of H_2 and Ar gases increases, the number of adsorbed atoms enhances. Consequently, probability of nucleation becomes higher on the substrate. At the moment of high flow rate of H_2 gas, the formation of MoO_{3-x} speeds up along with the excess Se vapor in reacting region, which makes more coverage of $MoSe_2$ flakes over the substrate. In case of low flow rate of H_2 gas, the amount of Se vapors can not transport sufficiently, and probability of $MoSe_2$ coverage over the substrate becomes lower. However, the shapes are not transformed into perfect ST, TT, REC, and hexagon at a low H_2 flow rate (MS-8). On the other hand, most regions are covered by the hexagons (MS-7) at a high flow rate of H_2 gas. The effect of H_2 flow on $MoSe_2$ flakes has been previously reported in detail by another research group.[27] Next, variation in temperature from 770 °C to 810 °C increases the evaporation rate of precursors which directly influence growing rate of Mo and Se edge. Consequently, difference in Mo and Se edge termination creates varying shapes on the substrate. Further, in the course of a high flow rate of Ar gas, smoothening on the flake side is minimized (MS-3). Moreover, as growth time increases, $MoSe_2$ flakes start to merge together and form the large area monolayer (MS-1 and MS-3). In addition to this, merging of flakes is also appeared in other samples owing to the high precursor's weight ratio (MoO_3 : Se). One would conclude from these observations, the shape of $MoSe_2$ flakes can be tailored by varying processing parameters.

Now, we turn our attention towards the crystal structure of monolayer $MoSe_2$ and different atomic arrangements in obtained shapes. The crystal structure of monolayer $MoSe_2$ consists of a 2D hexagonal lattice, where Mo and Se atoms are arranged in trigonal prismatic coordination (Fig. 3a). Further, the possible atomic arrangements in different as-synthesized shapes (ST, TT, hexagon, and REC) are represented in Fig. 3b–f. Fig. 3b and c show the atomic arrangements with Mo-zz termination and Se-zz termination in ST shape. One can observe the difference in the arrangement of Mo and Se atoms in TT, hexagon, and REC (see Fig. 3d–f). Based on the slowest and fastest-growing faces (Mo-zz and Se-zz), one can determine the shape of $MoSe_2$ flakes. The transformation from ST to REC shapes is a direct consequence of the surface energies of both Mo and Se edges. Apart from this, the variation in shape of $MoSe_2$ flakes is ascribed to the change in Mo : Se ratio of precursors.

In order to examine the quality and number of layers of as-synthesized $MoSe_2$ flakes, Raman spectroscopy has been carried out. Fig. 4a shows Raman spectra of as-synthesized $MoSe_2$ flakes over Si/SiO_2 and quartz substrate. The Raman spectra are captured at the center of the $MoSe_2$ flakes. The most pronounced single component peak (A_{1g}) has been found at 239.75 and 239.89 cm^{-1} in Si/SiO_2 and quartz substrate, respectively. One can observe the A_{1g} mode intensity is higher in Si/SiO_2 substrate than quartz substrate. The other major Raman modes are observed at 170.53 cm^{-1} (E_{1g}), 250.28 cm^{-1} (second-order Raman mode) and 286.93 cm^{-1} (E_{2g}^1) over Si/SiO_2 substrate. The $MoSe_2$ monolayer belongs to the space group D_{3h}^1 and in case of the monolayer, the irreducible representation
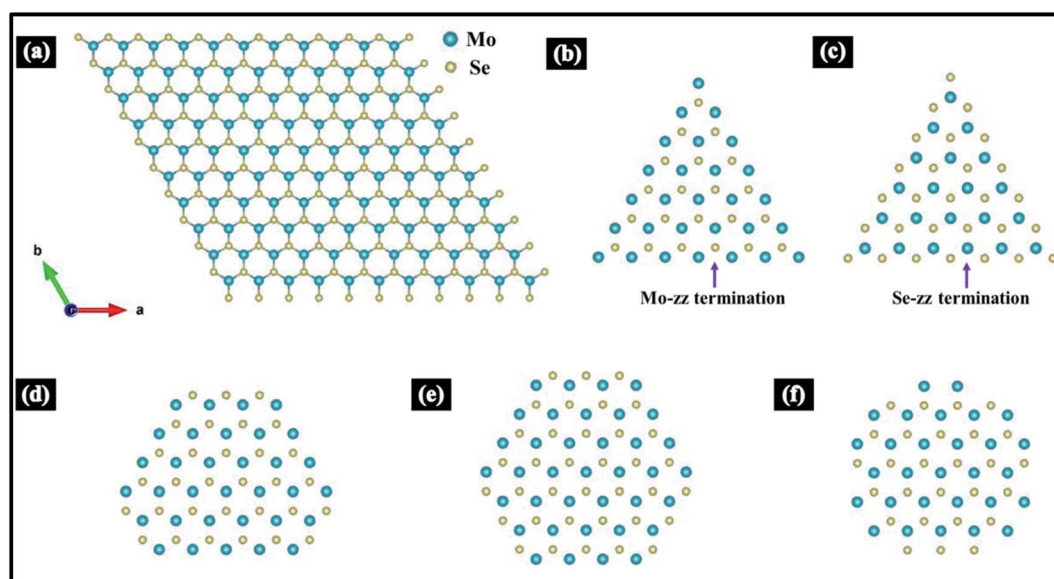

Fig. 3 (a) Top view of crystal structure of monolayer $MoSe_2$. The pictorial diagram of Mo and Se atomic arrangements in different shapes of as-synthesized monolayer $MoSe_2$ flakes: ST with (b) Mo-zz and (c) Se-zz termination; (d) TT, (e) hexagon, and (f) REC.
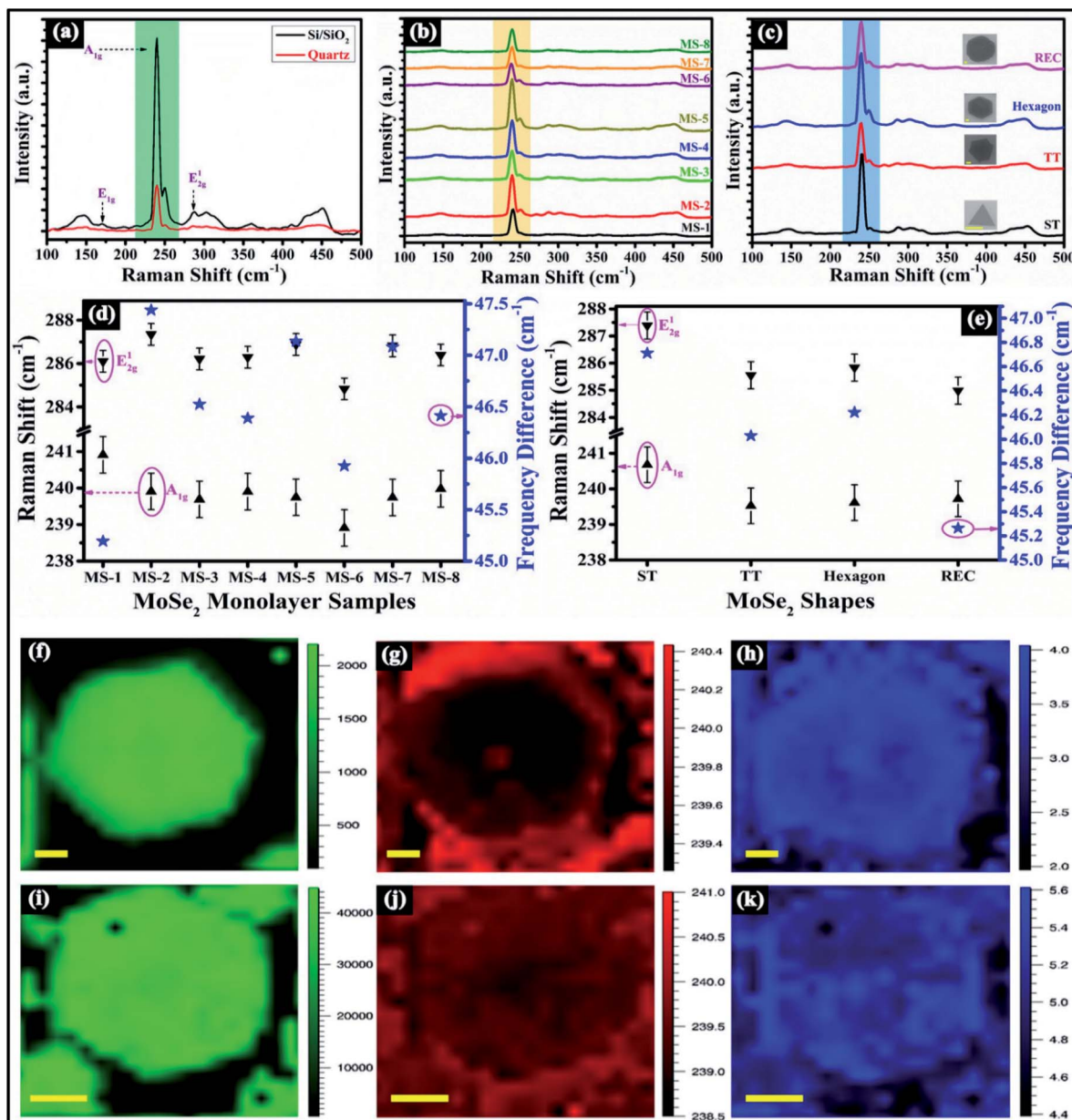
Fig. 4 (a) Raman spectrum of monolayer $MoSe_2$ flakes on the Si/SiO_2 and quartz substrate. (b) Raman spectra of different monolayer $MoSe_2$ samples (MS-1 to MS-8) over Si/SiO_2 substrate and vertically stacked for clarity. (c) Raman spectra of as-obtained shapes such as ST, TT, hexagon, and REC of monolayer $MoSe_2$ over Si/SiO_2 substrate. The Raman spectra are stacked vertically for clarity, and the scale bar in each shape is 2 µm. Peak position variation of A_{1g} and E_{2g}^1 Raman modes (left vertical axis) and their frequency difference (right vertical axis): (d) in as-synthesized samples and (e) in as-obtained shapes. Raman mapping in sample MS-3: (f) peak intensity, (g) peak position, and (h) peak width. Raman mapping in sample MS-5: (i) peak intensity, (j) peak position, and (k) peak width. The scale bar is 5 µm in each mapped image.

of the Γ phonons is described by $\Gamma = A'_1 + E'' + 2A''_2 + 2E'$. At Γ point, $MoSe_2$ monolayer has the nine-phonon modes having six-optical and three-acoustic branches.[28] The Raman active modes A_{1g} (A'_1) relates to the out of plane vibrations of Se atoms and E_{2g}^1 (E') is attributed to in plane vibrations of Mo and Se atoms. The E'' and A''_2 modes are not Raman active in monolayer. The peak appeared close to 250 cm^{-1} is second order Raman mode owing to double resonance process. The frequency difference between A_{1g} and peak close to 250 cm^{-1}, A_{1g} and E_{2g}^1 peaks are found to be ~10.53 cm^{-1} and ~47.18 cm^{-1}; the peak intensity

close to ~170 and ~360 cm^{-1} is found to be negligible as compared to A_{1g} peak (see Fig. 4a).These above mentioned features confirms that the synthesized $MoSe_2$ flakes are monolayer in nature and agrees well with the previous reports.[29,30] Fig. 4b and c displays Raman spectra of different samples (MS-1 to MS-8) and different as-obtained shapes, *i.e.*, ST, TT, hexagon, and REC of monolayer $MoSe_2$ at the center location. The frequency difference between A_{1g} and peak close to 250 cm^{-1} is found to be >10 cm^{-1} suggesting that the as-synthesized samples and as-obtained shapes are monolayers in nature.

The peak frequencies of A_{1g} and E_{2g}^1 Raman modes, along with their frequency differences in different as-synthesized samples and as-obtained shapes of monolayer $MoSe_2$ have been shown in Fig. 4d and e. The frequency difference between these two modes has been found to be >45 cm^{-1} which further confirms that the as-synthesized samples and as-obtained shapes are monolayers in nature.[30] The peak frequency of A_{1g} and E_{2g}^1 Raman modes vary from 239.52 to 240.91 cm^{-1} in as-synthesized samples and 284.83 to 287.38 cm^{-1} in as-obtained shapes, respectively. One can notice that the variation in experimental parameters does not affect the frequency of A_{1g} mode significantly. Moreover, to more thoroughly examine the uniformity of A_{1g} vibrational mode, Raman mapping has been employed. Fig. 4f–h illustrates Raman mapping in sample MS-3, and the intensity map shows the uniform color contrast at centre as well as edge, as depicted in Fig. 4f. The peak position map displays different color contrast at edge and middle region, as can be seen from Fig. 4g. The peak width map reveals the nearly uniform contrast except some regions nearby centre, as shown in Fig. 4h. Fig. 4i–k shows the Raman mapping in sample MS-5 and color contrast shows the small variation in few locations in peak intensity, peak position and peak width mapping. It can be noticed that Raman mapping of A_{1g} mode shows higher uniformity in MS-3 as compared to MS-5. These observations clearly confirm that the as-synthesized samples are high in quality. Further, AFM has been employed to examine the uniformity and thickness of monolayer $MoSe_2$ flakes over Si/SiO$_2$ substrate, which is shown in Fig. S3 (in the ESI).† Next, TEM has been carried out to examine the crystalline structure of CVD-grown $MoSe_2$ flakes. Fig. 5a shows the bright field plan-view TEM image of $MoSe_2$ flake having REC shape at low magnification. The high-resolution TEM (HRTEM) image is shown in Fig. 5b, and inset shows the enhanced view of lattice fringe which is marked by rectangular region. The lattice spacing is measured from the HRTEM image and found to be ~0.28 nm, which corresponds to {10$\bar{1}$0} planes. Fig. 5c displays the selected area electron diffraction (SAED) pattern within the REC shape, having one set of diffraction spots with six-fold symmetry. These features confirm that the synthesized monolayer $MoSe_2$ flakes are single crystalline in nature. From the
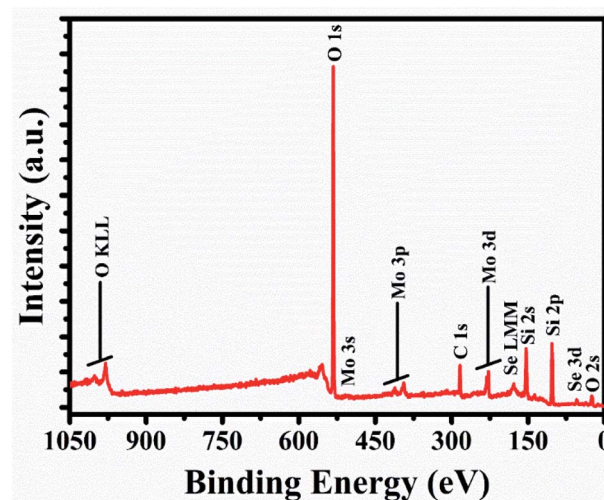

Fig. 6 Survey scan is captured on the as-synthesized monolayer $MoSe_2$ flakes deposited on the Si/SiO$_2$ substrate. The identified elements are marked.

SAED pattern, one can also compute the lattice spacing corresponds to {10$\bar{1}$0} and {11$\bar{2}$0} planes, which are determined to be ~0.28 nm and ~0.16 nm and agree well with previous reports.[2,10,24] Furthermore, to examine the oxidation states and atomic ratio in an as-synthesized monolayer $MoSe_2$, X-ray photoelectron spectroscopy (XPS) has been carried out. The survey scan of as-synthesized $MoSe_2$ flakes deposited over Si/SiO$_2$ substrate is displayed in Fig. 6. The core-level spectra of Mo 3d and Se 3d are displayed in Fig. 7a and b. The spectra are fitted with the Gaussian–Lorentzian function, and the estimated background is Shirley type. The Mo 3d spin–orbit doublet comprises two peaks Mo 3d$_{5/2}$ ~ 228.5 eV and Mo 3d$_{3/2}$ ~ 231.8 eV, which corresponds to Mo^{4+} 3d states.

Additionally, a relatively more minor amount of MoO_3 is expectedly present in $MoSe_2$ flakes, confirmed by the appearance of the binding energy peaks at 232.7 eV (3d$_{5/2}$) and 235.7 eV (3d$_{3/2}$) of Mo^{6+} charge states and agrees well with Mo^{6+} oxidation state from α-MoO_3.[31] The Se 3d spectra at the binding energy of ~54.7 eV and 55.7 eV relate with the doublets core
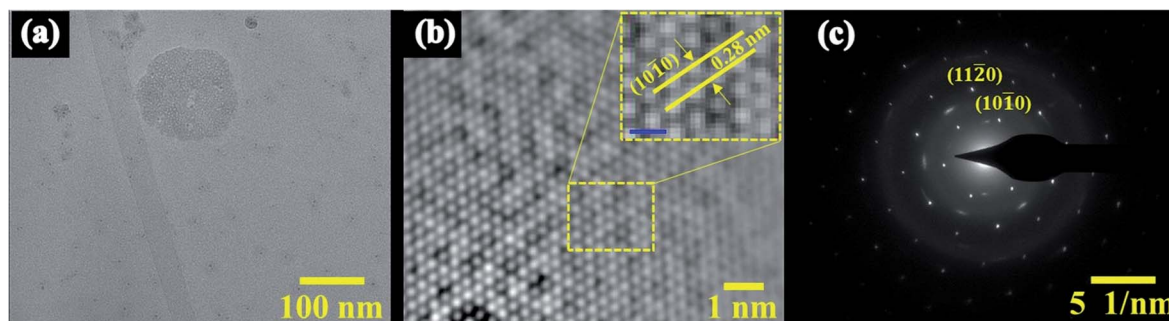

Fig. 5 (a) The bright-field TEM image of transferred monolayer $MoSe_2$ flake having REC shape. (b) HRTEM image of the REC shape and inset shows the enhanced view of the atomic arrangement of Mo and Se atoms with a scale bar of 0.5 nm. (c) SAED pattern confirms the hexagonal symmetry of the $MoSe_2$ structure.
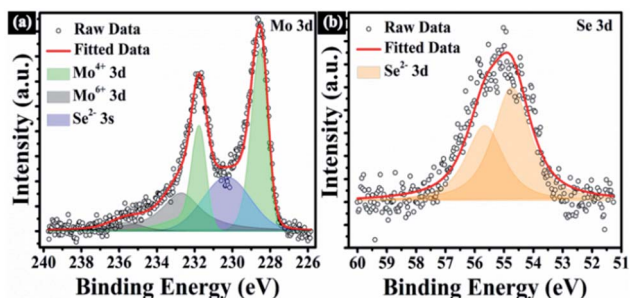
Fig. 7 High-resolution XPS spectra of (a) Mo 3d and (b) Se 3d recorded at room temperature.

level $3d_{5/2}$ and $3d_{3/2}$, which belongs to the Se^{2-} oxidation state of selenium.

One can observe that the Mo^{6+} 3d state and Se^{2-} 3s state overlap with the Mo^{4+} 3d states.[32] The above-mentioned features closely match with the earlier published literature of CVD-grown monolayer $MoSe_2$.[10,33,34] In order to estimate the atomic ratio, the integrated peak areas of Mo^{4+} 3d and Se^{2-} 3d peaks have been taken into consideration, and peak areas are normalized with respect to the atomic sensitivity factor. The estimated Se/Mo ratio is found to be ~1.8, indicating a large amount of Se vacancies are present in as-synthesized $MoSe_2$ flakes.

Further, in order to determine the optical transitions, the absorption spectrum is collected on monolayer $MoSe_2$ flakes over the quartz substrate, as shown in Fig. S4 (in the ESI).†

Moreover, photoluminescence is another robust technique to characterize the quality of the as-synthesized $MoSe_2$ flakes. Fig. 8a shows the PL spectra of monolayer $MoSe_2$ over Si/SiO_2 and quartz substrate at room temperature. The prominent emission peak is found to be at ~799.35 nm (1.55 eV) on Si/SiO_2 and ~792.58 nm (1.56 eV) on a quartz substrate. The strong emission peak is attributed to the direct transition at the K point of the Brillouin zone, and the direct band gap emission is corroborated with the previous reports of the monolayer $MoSe_2$.[24,27] A red shift has been observed in PL peak position on Si/SiO_2 substrate, and PL intensity is reduced approximately

seven times compared to the quartz substrate. The strong PL intensity on quartz substrate is owing to the availability of rich electron density, which induces more excitons formation. It is worth noting that a broader tail at high wavelength side and a steep edge at the lower wavelength side in PL emission. Furthermore, Fig. 8b and c illustrate the PL spectra of different as-synthesized samples and as-obtained shapes. In each sample, the PL spectrum is recorded at the center of flake. In both the figures, displayed spectra are collected at one location of monolayer $MoSe_2$. It is interesting to note that the PL intensity of MS-7 is more pronounced as compared to other samples (see Fig. 8b). On the other side, REC shape exhibits most prominent PL feature among all the obtained shapes. The peak position of A exciton along with the normalized PL in as-synthesized samples and as-obtained shapes is displayed in Fig. S5a and b (in the ESI).† The significant shift has been observed in A exciton peak energy which is in range of ~1.52–1.57 eV, as described in Fig. S5a (in the ESI).† It can be noticed that A exciton peak is observed in the range of ~1.506–1.514 eV in as-obtained shapes. The as-obtained shapes which are displayed in Fig. S5b (in the ESI),† belong to sample MS-6. In addition to this, the distinct shapes have been analyzed in each sample and found that the A exciton peak lies within the range of ~1.50–1.58 eV, 1.50–1.52 eV, 1.50–1.56 eV, and 1.51–1.57 eV for ST, TT, hexagon, and REC shapes respectively. The excitonic quasi-particles (excitons and trions) exist together at room temperature by virtue of strong Coulomb interactions in 2D materials.

The appearance of prominent excitonic features in the monolayer is attributed to the large binding energies. The large exciton binding energy occurs because of the geometrical confinement of excitonic quasiparticles in low dimensional systems, which enhance the e–h overlapping.[35,36] Additionally, the interaction between charges becomes stronger as the thickness goes down; as a consequence screening effects become lower and induces the strong electron–electron correlation.[37] Moreover, to examine the contribution of neutral exciton (A^0) and trions (A^-) in strong PL emission, the PL spectra are fitted with two Voigt functions, as shown in Fig. 9a–l. The PL emission of trion is red shifted in each case, ascribed to
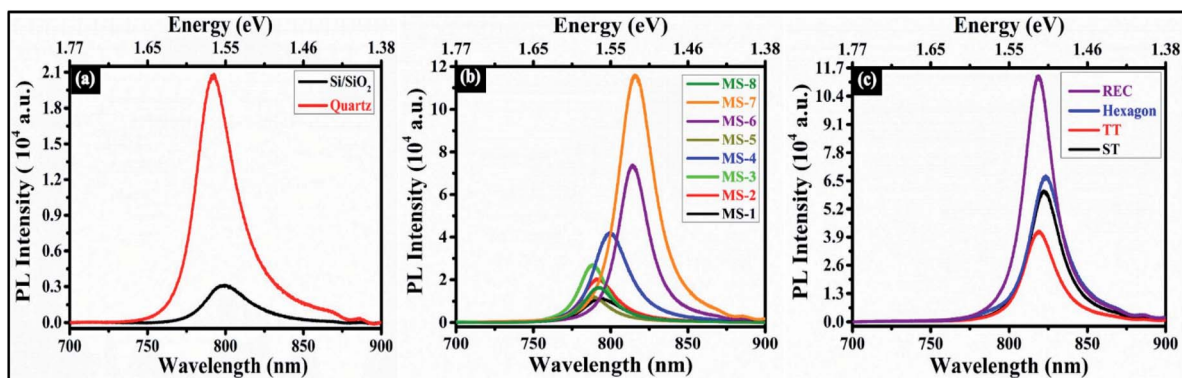

Fig. 8 (a) PL spectrum of monolayer $MoSe_2$ flakes over Si/SiO_2 and quartz substrate. (b) PL spectra of different monolayer $MoSe_2$ samples (MS-1 to MS-8) over Si/SiO_2 substrate. (c) PL spectra of as-obtained shapes of monolayer $MoSe_2$ flakes.
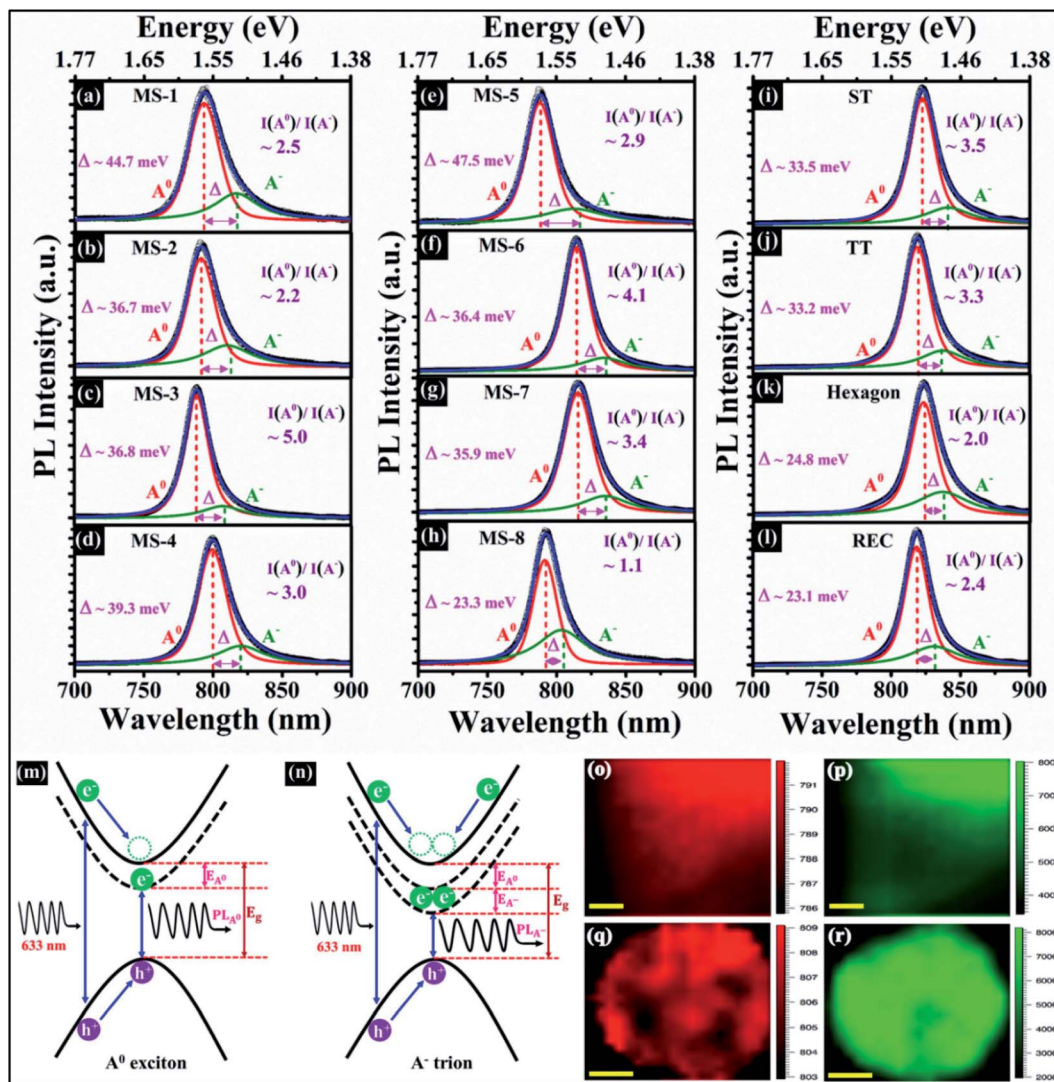
Fig. 9 PL spectra are deconvoluted for obtaining the neutral exciton and charge exciton contribution: (a–h) as-synthesized samples (MS-1 to MS-8) and (i–l) as-obtained shapes. Experimental data, fitted data, A^0 exciton PL peak, and A^- trion PL peak are represented by circular dots (black), blue lines, red lines, and green lines, respectively, where Δ is the energy difference between A^0 exciton and A^- trion. Schematic diagram of the excitonic transitions: (m) A^0 exciton formation and (n) A^- trion formation. Here E_{A^0}, E_{A^-}, E_g, PL_{A^0}, and PL_{A^-}, denote the A^0 exciton binding energy, A^- trion binding energy, electronic band gap, PL peak energy of A^0 exciton, and A^- trion. In the case of A^0, the electronic band gap (E_g) is the sum of PL peak energy (PL_{A^0}) and the neutral exciton binding energy (E_{A^0}), which is expressed as $E_g = PL_{A^0} + E_{A^0}$. For charged exciton (trion), the electronic band gap is described as $E_g = PL_{A^-} + E_{A^0} + E_{A^-}$. PL mapping in the edge of large-area monolayer $MoSe_2$: (o) peak position and (p) peak intensity. PL mapping in the REC shape: (q) peak position and (r) peak intensity.

electron–phonon interaction. The trion emission is lower than neutral exciton emission in all the synthesized samples and different obtained shapes, depicted in Fig. 9a–l. The quasiparticle's intensity ratio {area ratio, $I(A^0)/I(A^-)$} has been found ≥ 2 in all the synthesized samples and obtained shapes except sample MS-8. In sample MS-8, $I(A^0)/I(A^-)$ is found to be ~ 1.1, suggesting that the emission of trion is almost comparable to neutral exciton emission. These observations indicate that the stronger radiative recombination takes place in samples MS-1 to MS-7 and as-obtained shapes in comparison to MS-8. The obvious difference in $I(A^0)/I(A^-)$ as a consequence of the varying experimental conditions. Generally, variation in growth temperature generates a significant strain on the substrate due

to which the deposited monolayer flakes are affected. In addition, the different concentration of precursors in vaporized form induce varying defect structures in as-synthesized shapes. Previously, it has been observed that the extra charges originate from doping, defects, substrate, and gate biasing.[38,39] To gain more physical insight into trion binding energy, the calculation of energy difference (Δ) between A^0 and A^- is required. The PL peak energy position of neutral exciton and trion has been illustrated in Fig. S5c (in the ESI)† for the as-synthesized samples. The energy difference (Δ) between A^0 exciton and A^- trion is found to be 23.3–47.5 meV. Similarly, the excitonic peak positions in as-obtained shapes have been shown in Fig. S5d (in the ESI),† and energy difference is observed in the range of 23.1–

33.5 meV, respectively. Previously, it has been seen that trion binding energy is approximately 0.1 times the exciton binding energy in monolayer TMDCs.[40] In the present study, obtained trion binding energy in as-synthesized samples and as-obtained shapes are closely matched with the earlier report[39] and the small shift in trion binding energy as a result of varying electron–phonon coupling strengths. These results point out that the behavior of neutral and charged exciton in PL spectra is significantly affected by experimental conditions. Moreover, Fig. 9m and n display schematic energy band diagram of neutral exciton (A^0) and trion (A^-). In case of A^0, the electronic band gap (E_g) is sum of PL peak energy (PL_{A^0}) and neutral exciton binding energy (E_{A^0}), which is expressed as $E_g = PL_{A^0} + E_{A^0}$. Now, in case of charged exciton (trion), electronic band gap is described as $E_g = PL_{A^-} + E_{A^0} + E_{A^-}$, where E_{A^-} is the binding energy of A^- trion. Here, excitation energy of 1.96 eV is used to capture PL spectra and which is larger than the band gap. When the bound e^- is promoted in the conduction band *via* interaction of light, the high energy e^- loses energy in form of thermal energy and settles down in the minimum energy state in the conduction band (conduction band minimum), as shown in Fig. 9m and n. As similar, the thermalization loss occurs in valence band also, holes move towards their minimum energy state, which is the top of valence band (valence band maximum).

However, in semiconductors, there are two mechanisms of exciton formation which are mainly taken into consideration: (a) high kinetic energy exciton generates the photon along with phonon emission concurrently, the e–h recapitulate during this process;[41] (b) formation of bi-molecular exciton.[42] But in case of monolayer TMDCs, the recapitulation of e–h only takes place when excitation energy is lower than the free particle band gap. When carrier densities becomes high, probability of the scattering (elastic or inelastic) with free carriers is enhanced. A new state comes in to the existence as inelastic scattering occurs between free charge carriers and exciton. Throughout this process, excitons gained extra charge and created the trion states. Furthermore, PL mapping has been carried out over $MoSe_2$ flakes to probe the crystal quality. Fig. 9o–r shows the PL maps with respect to peak position and peak intensity of A exciton in edge of large area $MoSe_2$. The color contrast of peak position map exhibits boundary of a large area, which has a slight difference as compared to centre of a large area, as shown in Fig. 9o. In the peak intensity map, PL intensity becomes lowers towards boundary of a large area and enhances at the central part, illustrated in Fig. 9p. The PL peak position and peak intensity images of A excitonic peak in REC shape have been illustrated in Fig. 9q and r. The color contrast of REC shape displays the uniform region except few darker regions where the PL peak positions are blue shifted (see Fig. 9q). The PL intensity map reveals that intensity is uniform in almost all the regions aside from some of the small patches, as can be seen from Fig. 9r. In addition, PL peak position and peak intensity maps on the distorted hexagonal shape have been shown in Fig. S6 (in the ESI).† The PL position and intensity maps imply that the as-synthesized samples are high in quality and monolayer in nature.

Hence, present work offers a platform for the optical tuning of excitonic emission in CVD-grown monolayer $MoSe_2$ and exploring the applications in field of optoelectronics and valleytronics.

Conclusions

In summary, we have been synthesized high-quality monolayer $MoSe_2$ flakes using a lab-built CVD setup, and a range of shapes, namely sharp triangle, truncated triangle, hexagon, rough edge circle, have been evolved in the course of growth at different optimized conditions. The obtained morphologies of monolayer $MoSe_2$ confirmed that the processing parameters, including growth temperature, gas flow rate, substrate's location, and growth time, played a crucial role in controlling the quality of samples. An extensive study of Raman scattering in as-synthesized samples (MS-1 to MS-8) and as-obtained shapes have been presented and confirming that prepared samples are highly uniform and monolayer in nature. Further, prominent PL emission at room temperature confirms the monolayer nature of synthesized $MoSe_2$ flakes, where peak energy of A exciton is found to be in the range of 1.50–1.58 eV. Moreover, binding energy of trion is evaluated in monolayer $MoSe_2$ and found to be in the range of 23.1–47.5 meV. The spectral weight of exciton and trion in PL emission directly affects the process of radiative recombination. In addition, the emission of trion has been found very weak as compared to the neutral exciton emission in most synthesized samples. Thus, this study opens up new avenues to get insight into lattice and quasiparticles dynamics under the influence of processing parameters and may pave the way in controlling the optical properties.

Author contributions

Girija Shankar Papanai – conceptualization, investigation, methodology, formal analysis, writing-original draft. Krishna Rani Sahoo – Raman and PL measurements, review and editing. Betsy Reshma G – AFM measurements. Sarika Gupta – AFM measurements, review and editing. Bipin Kumar Gupta – supervision, funding acquisition, conceptualization, validation, review and editing.

Conflicts of interest

There are no conflicts to declare.

Acknowledgements

Notes and references

1 L. Yang, C. Xie, J. Jin, R. Ali, C. Feng, P. Liu and B. Xiang, Properties, Preparation and Applications of Low Dimensional Transition Metal Dichalcogenides, *Nanomaterials*, 2018, **8**, 463.

2 J. Xia, X. Huang, L.-Z. Liu, M. Wang, L. Wang, B. Huang, D.-D. Zhu, J.-J. Li, C.-Z. Gu and X.-M. Meng, CVD synthesis of large-area, highly crystalline $MoSe_2$ atomic layers on diverse substrates and application to photodetectors, *Nanoscale*, 2014, **6**, 8949.

3 H. Chen, Y. Xie, H. Cui, W. Zhao, X. Zhu, Y. Wang, X. Lü and F. Huang, In situ growth of a $MoSe_2$/Mo counter electrode for high efficiency dye-sensitized solar cells, *Chem. Commun.*, 2014, **50**, 4475–4477.

4 Y. Liu, Y. Qu, Y. Liu, H. Yin, J. Liu, Y. Tan and F. Chen, Direct-Writing of 2D Diodes by Focused Ion Beams, *Adv. Funct. Mater.*, 2021, **31**, 2102708.

5 H. Ilatikhameneh, G. Klimeck, J. Appenzeller and R. Rahman, Design Rules for High Performance Tunnel Transistors From 2-D Materials, *IEEE J. Electron Devices Soc.*, 2016, **4**, 260–265.

6 S. Tongay, J. Zhou, C. Ataca, K. Lo, T. S. Matthews, J. Li, J. C. Grossman and J. Wu, Thermally Driven Crossover from Indirect toward Direct Bandgap in 2D Semiconductors: $MoSe_2$ versus MoS_2, *Nano Lett.*, 2012, **12**, 5576–5580.

7 S. Manzeli, D. Ovchinnikov, D. Pasquier, O. V. Yazyev and A. Kis, 2D transition metal dichalcogenides, *Nat. Rev. Mater.*, 2017, **2**, 17033.

8 X. Wu, Y. Wang, P. Li and Z. Xiong, Research status of $MoSe_2$ and its composites: a review, *Superlattices Microstruct.*, 2020, **139**, 106388.

9 X. Lu, M. I. B. Utama, J. Lin, X. Gong, J. Zhang, Y. Zhao, S. T. Pantelides, J. Wang, Z. Dong, Z. Liu, W. Zhou and Q. Xiong, Large-Area Synthesis of Monolayer and Few-Layer $MoSe_2$ Films on SiO_2 Substrates, *Nano Lett.*, 2014, **14**, 2419–2425.

10 X. Wang, Y. Gong, G. Shi, W. L. Chow, K. Keyshar, G. Ye, R. Vajtai, J. Lou, Z. Liu, E. Ringe, B. K. Tay and P. M. Ajayan, Chemical Vapor Deposition Growth of Crystalline Monolayer $MoSe_2$, *ACS Nano*, 2014, **8**, 5125–5131.

11 T. Chen, G. Hao, G. Wang, B. Li, L. Kou, H. Yang, X. Zheng and J. Zhong, Controlled growth of atomically thin $MoSe_2$ films and nanoribbons by chemical vapor deposition, *2D Mater.*, 2019, **6**, 025002.

12 M. Kim, J. Seo, J. Kim, J. S. Moon, J. Lee, J.-H. Kim, J. Kang and H. Park, High-Crystalline Monolayer Transition Metal Dichalcogenides Films for Wafer-Scale Electronics, *ACS Nano*, 2021, **15**, 3038–3046.

13 S. Li, S. Wang, T. Xu, H. Zhang, Y. Tang, S. Liu, T. Jiang, S. Zhou and H. Cheng, Growth mechanism and atomic structure of group-IIA compound-promoted CVD-synthesized monolayer transition metal dichalcogenides, *Nanoscale*, 2021, **13**, 13030–13041.

14 Z. Zhang, L. Zhu, D. Wang, B. Tang, P. Yang, Y. Shi, F. Zhou, J. Fu, Y. Huan, F. Cui, N. Li, Q. Chen, X. Zou, F. Chen and Y. Zhang, Ultrafast Growth of Large-Area Uniform, Millimeter-Size $MoSe_2$ Single Crystals on Low-Cost Soda-Lime Glass, *Adv. Mater. Interfaces*, 2021, **8**, 2100415.

15 H. M. Oh, G. H. Han, H. Kim and M. S. Jeong, Influence of residual promoter to photoluminescence of CVD grown MoS_2, *Curr. Appl. Phys.*, 2016, **16**, 1223–1228.

16 H. Kim, G. H. Han, S. J. Yun, J. Zhao, D. H. Keum, H. Y. Jeong, T. H. Ly, Y. Jin, J.-H. Park, B. H. Moon, S.-W. Kim and Y. H. Lee, Role of alkali metal promoter in enhancing lateral growth of monolayer transition metal dichalcogenides, *Nanotechnology*, 2017, **28**, 36LT01.

17 Y. Zhao, H. Lee, W. Choi, W. Fei and C. J. Lee, Large-area synthesis of monolayer $MoSe_2$ films on SiO_2/Si substrates by atmospheric pressure chemical vapor deposition, *RSC Adv.*, 2017, **7**, 27969–27973.

18 Y. Liu, Q. Zhou, Y. Yan, L. Li, J. Zhu, Y. Zheng, X. Huang, Y. Huang, F. Li and T. Cui, Wrinkle and near-resonance effects on the vibrational and electronic properties in compressed monolayer $MoSe_2$, *Phys. Chem. Chem. Phys.*, 2021, **23**, 11709–11716.

19 K. Hao, L. Xu, P. Nagler, A. Singh, K. Tran, C. K. Dass, C. Schüller, T. Korn, X. Li and G. Moody, Coherent and Incoherent Coupling Dynamics between Neutral and Charged Excitons in Monolayer $MoSe_2$, *Nano Lett.*, 2016, **16**, 5109–5113.

20 A. Singh, G. Moody, S. Wu, Y. Wu, N. J. Ghimire, J. Yan, D. G. Mandrus, X. Xu and X. Li, Coherent Electronic Coupling in Atomically Thin $MoSe_2$, *Phys. Rev. Lett.*, 2014, **112**, 216804.

21 T. Godde, D. Schmidt, J. Schmutzler, M. Aßmann, J. Debus, F. Withers, E. M. Alexeev, O. Del Pozo-Zamudio, O. V. Skrypka, K. S. Novoselov, M. Bayer and A. I. Tartakovskii, Exciton and trion dynamics in atomically thin $MoSe_2$ and WSe_2: effect of localization, *Phys. Rev. B*, 2016, **94**, 165301.

22 N. Kumar, Q. Cui, F. Ceballos, D. He, Y. Wang and H. Zhao, Exciton-exciton annihilation in $MoSe_2$ monolayers, *Phys. Rev. B: Condens. Matter Mater. Phys.*, 2014, **89**, 125427.

23 G. S. Papanai, S. Pal, P. Pal, B. S. Yadav, P. Garg, S. Gupta, S. G. Ansari and B. K. Gupta, New insight into the growth of monolayer MoS_2 flakes using an indigenously developed CVD setup: a study on shape evolution and spectroscopy, *Mater. Chem. Front.*, 2021, **5**, 5429–5441.

24 J. C. Shaw, H. Zhou, Y. Chen, N. O. Weiss, Y. Liu, Y. Huang and X. Duan, Chemical vapor deposition growth of monolayer $MoSe_2$ nanosheets, *Nano Res.*, 2014, **7**, 511–517.

25 X. L. Li and Y. D. Li, Formation of MoS_2 Inorganic Fullerenes (IFs) by the Reaction of MoO_3 Nanobelts and S, *Chem.–Eur. J.*, 2003, **9**, 2726–2731.

26 H. Ye, J. Zhou, D. Er, C. C. Price, Z. Yu, Y. Liu, J. Lowengrub, J. Lou, Z. Liu and V. B. Shenoy, Toward a Mechanistic Understanding of Vertical Growth of van der Waals Stacked 2D Materials: A Multiscale Model and Experiments, *ACS Nano*, 2017, **11**, 12780–12788.

27 Y. Li, K. Zhang, F. Wang, Y. Feng, Y. Li, Y. Han, D. Tang and B. Zhang, Scalable Synthesis of Highly Crystalline $MoSe_2$ and Its Ambipolar Behavior, *ACS Appl. Mater. Interfaces*, 2017, **9**, 36009–36016.

28 X. Lu, X. Luo, J. Zhang, S. Y. Quek and Q. Xiong, Lattice vibrations and Raman scattering in two-dimensional layered materials beyond graphene, *Nano Res.*, 2016, **9**, 3559–3597.

29 P. Soubelet, A. E. Bruchhausen, A. Fainstein, K. Nogajewski and C. Faugeras, Resonance effects in the Raman scattering of monolayer and few-layer $MoSe_2$, *Phys. Rev. B*, 2016, **93**, 155407.

30 K. Kim, J.-U. Lee, D. Nam and H. Cheong, Davydov Splitting and Excitonic Resonance Effects in Raman Spectra of Few-Layer $MoSe_2$, *ACS Nano*, 2016, **10**, 8113–8120.

31 J. Li and X. Liu, Fabrication and enhanced electrochemical properties of α-MoO_3 nanobelts using dodecylbenzenesulfonic acid as both reactant and surfactant, *CrystEngComm*, 2014, **16**, 184–190.

32 A. Azcatl, S. Kc, X. Peng, N. Lu, S. McDonnell, X. Qin, F. de Dios, R. Addou, J. Kim, M. J. Kim, K. Cho and R. M. Wallace, HfO_2 on UV–O_3 exposed transition metal dichalcogenides: interfacial reactions study, *2D Mater.*, 2015, **2**, 014004.

33 S. Chowdhury, A. Roy, I. Bodemann and S. K. Banerjee, Two-Dimensional to Three-Dimensional Growth of Transition Metal Diselenides by Chemical Vapor Deposition: Interplay between Fractal, Dendritic, and Compact Morphologies, *ACS Appl. Mater. Interfaces*, 2020, **12**, 15885–15892.

34 S. Wang, G. Wang, X. Yang, H. Yang, M. Zhu, S. Zhang, G. Peng and Z. Li, Synthesis of Monolayer $MoSe_2$ with Controlled Nucleation via Reverse-Flow Chemical Vapor Deposition, *Nanomaterials*, 2019, **10**, 75.

35 P. Lefebvre, P. Christol and H. Mathieu, Unified formulation of excitonic absorption spectra of semiconductor quantum wells, superlattices, and quantum wires, *Phys. Rev. B: Condens. Matter Mater. Phys.*, 1993, **48**, 17308–17315.

36 X.-F. He, Excitons in anisotropic solids: the model of fractional-dimensional space, *Phys. Rev. B: Condens. Matter Mater. Phys.*, 1991, **43**, 2063–2069.

37 C. Delerue, G. Allan and M. Lannoo, Dimensionality-Dependent Self-Energy Corrections and Exchange-Correlation Potential in Semiconductor Nanostructures, *Phys. Rev. Lett.*, 2003, **90**, 076803.

38 B. Radisavljevic, A. Radenovic, J. Brivio, V. Giacometti and A. Kis, Single-layer MoS_2 transistors, *Nat. Nanotechnol.*, 2011, **6**, 147–150.

39 J. S. Ross, S. Wu, H. Yu, N. J. Ghimire, A. M. Jones, G. Aivazian, J. Yan, D. G. Mandrus, D. Xiao, W. Yao and X. Xu, Electrical control of neutral and charged excitons in a monolayer semiconductor, *Nat. Commun.*, 2013, **4**, 1474.

40 M. Van der Donck, M. Zarenia and F. M. Peeters, Excitons and trions in monolayer transition metal dichalcogenides: a comparative study between the multiband model and the quadratic single-band model, *Phys. Rev. B*, 2017, **96**, 035131.

41 A. Bonnot, R. Planel and C. B. à la Guillaume, Optical orientation of excitons in CdS, *Phys. Rev. B: Solid State*, 1974, **9**, 690–702.

42 C. Piermarocchi, F. Tassone, V. Savona, A. Quattropani and P. Schwendimann, Exciton formation rates in GaAs/$Al_xGa_{1-x}As$ quantum wells, *Phys. Rev. B: Condens. Matter Mater. Phys.*, 1997, **55**, 1333–1336.